




**Ferroelectric tuning of superconductivity and band topology in a two-dimensional heterobilayer**Jianyong Chen <sup>1,2</sup>, Wei Qin,<sup>1,3</sup> Ping Cui <sup>1,4,\*</sup> and Zhenyu Zhang <sup>1,4,†</sup><sup>1</sup>*International Center for Quantum Design of Functional Materials (ICQD),**Hefei National Research Center for Physical Sciences at Microscale,**University of Science and Technology of China, Hefei, Anhui 230026, China*<sup>2</sup>*College of Science, Guilin University of Aerospace Technology, Guilin 541004, China*<sup>3</sup>*Department of Physics, University of Science and Technology of China, Hefei, Anhui 230026, China*<sup>4</sup>*Hefei National Laboratory, University of Science and Technology of China, Hefei 230088, China*

(Received 19 February 2022; revised 23 May 2023; accepted 20 June 2023; published 4 August 2023)

Realization of tunable superconductivity with concomitant nontrivial band topology is conceptually intriguing and highly desirable for next-generation nanoscale superconducting devices. Based on first-principles calculations, here we present a prediction of simultaneously tunable superconducting transition temperature ( $T_c$ ) and band topology in a superconducting IrTe<sub>2</sub> overlayer on a ferroelectric In<sub>2</sub>Se<sub>3</sub> monolayer. We first demonstrate that the  $T_c$  is substantially enhanced from that of IrTe<sub>2</sub> nanoflakes ( $T_c \sim 3$  K) due to significant charge repartitioning around the Fermi level. More importantly, the  $T_c$  is shown to sensitively depend on the In<sub>2</sub>Se<sub>3</sub> polarization, with the higher  $T_c$  of  $\sim(8-10)$  K attributed to enhanced interlayer electron-phonon coupling when the polarization is downward. The band topology is also switched from trivial to nontrivial as the polarization is reversed from upward to downward. These findings provide physically realistic platforms for simultaneously tuning superconductivity and band topology in two-dimensional heterobilayers and related heterostructures using a reversible and nonvolatile approach, with immense application potential for superconducting diodes and topological quantum computation.

DOI: [10.1103/PhysRevB.108.L060501](https://doi.org/10.1103/PhysRevB.108.L060501)

Achieving tunable superconductivity is a prerequisite for fabrication of reprogrammable superconducting circuits and utilization of magnetic flux quanta [1,2]. Ferroelectric effects, as characterized by switchable polarization of a ferroelectric material upon application of a voltage pulse, can be exploited as a nonvolatile and reversible approach to modulate the superconducting transition temperature ( $T_c$ ). Such ferroelectric tuning of superconductivity has been achieved in heterostructures of traditional superconducting and ferroelectric films. Representative examples include significant  $T_c$  modulations in Pb(Zr<sub>x</sub>Ti<sub>1-x</sub>)O<sub>3</sub>/GdBa<sub>2</sub>Cu<sub>3</sub>O<sub>7-x</sub> [3] and BiFeO<sub>3</sub>/YBa<sub>2</sub>Cu<sub>3</sub>O<sub>7-x</sub> [4], and a complete switching of a superconducting transition in Nb-doped SrTiO<sub>3</sub> with Pb(Zr, Ti)O<sub>3</sub> as the ferroelectric overlayer [5].

Traditional superconductor/ferroelectric heterostructures are typically hampered by nonuniform film thickness, structural imperfections, random interfacial charge traps, and relatively broad superconducting transitions due to the two-dimensional (2D) nature of the interfacial superconductivity [6,7]. Since the ferroelectric effects are more pronounced near the interfaces [8], atomically thin superconductors are expected to be more substantially tunable. In this regard, the concurrent discoveries of 2D ferroelectric [9–14] and superconducting [15–18] materials offer unprecedented

opportunities for exploration of ferroelectrically tuned superconductivity and related devices, especially given the atomically sharp interfacial qualities of such van der Waals (vdW) heterostructures [19,20]. These layered systems, in turn, may also enable realizations of other emergent physical properties and functionalities, including, notably, topological superconductivity for fault-tolerant topological quantum computing.

In this Letter, using first-principles approaches, we demonstrate that the superconducting transition temperature and band topology of a two-dimensional IrTe<sub>2</sub> superconductor can be simultaneously tuned via proximity coupling with a ferroelectric In<sub>2</sub>Se<sub>3</sub> monolayer. We show that the  $T_c$ 's of the heterobilayers are substantially enhanced compared to the IrTe<sub>2</sub> nanoflakes, which can be attributed to significant charge repartitioning around the Fermi level. More intriguingly, the  $T_c$  sensitively depends on the In<sub>2</sub>Se<sub>3</sub> polarization, with the higher  $T_c$  caused by enhanced interlayer electron-phonon coupling (EPC) for the downward polarization. Furthermore, the band topology is switchable from trivial to nontrivial as the polarization is reversed from upward to downward, resulting from the cooperative effects of proper band alignments and inherently strong spin-orbit coupling (SOC). These findings provide physically realistic platforms for simultaneously tuning superconductivity and band topology in 2D heterostructures using a superior ferroelectric tuning knob that is nonvolatile, bistable, and allows for high spatial precision tunability. The nonvolatile aspect serves as the basis for much faster and low-power tuning, while the bistabil-

\* cuipeg@ustc.edu.cn

† zhangzy@ustc.edu.cn

ity can be exploited for more reliable and tunable quantum states. The higher spatial precision in the tunability is inherently tied to nanoscale ferroelectric domain sizes in 2D ferroelectric systems, a vital aspect to be elaborated upon later. Overall, our study provides appealing platforms for simultaneously and reversibly tuning superconductivity and band topology in 2D heterostructures, with significant application potential in superconducting devices and topological quantum computing.

First-principles calculations were mainly performed using the QUANTUM-ESPRESSO materials simulation suite [21]. The Perdew-Burke-Ernzerhof (PBE) of the parametrized generalized-gradient approximation (GGA) [22] was used to describe the exchange correlation. The vdW interlayer coupling was treated by the semiempirical correction based on the Grimme's scheme (PBE-D2) [23–25]. A plane-wave basis with a 70 Ry energy cutoff was used to represent electronic wave functions. The dynamical matrices were calculated using the density functional perturbation theory (DFPT) [26] in the linear response regime on an  $8 \times 8 \times 1$  Monkhorst-Pack (MP) [27]  $q$ -point grid. The EPC strengths converge when adopting a fine grid of  $24 \times 24 \times 1$   $k$  points with a Marzari-Vanderbilt [28] smearing of 0.02 Ry. The superconducting transition temperature is evaluated by the McMillan-Allen-Dynes formula [29,30]. The edge Green's functions [31] were obtained by using the maximally localized Wannier functions as implemented in the WANNIERTOOLS package [32] and WANNIERTOOLS code [33].

The  $\text{IrTe}_2$  and  $\text{In}_2\text{Se}_3$  monolayers share a similar triangular atomic arrangement within each atomic layer, with the lattice constants of 3.84 and 4.10 Å, respectively. An  $\text{IrTe}_2/\text{In}_2\text{Se}_3$  heterobilayer can adopt a  $(1 \times 1)$  matching relationship with a  $\sim 6\%$  mismatch, by treating  $\text{In}_2\text{Se}_3$  as the substrate. With three high-symmetry stacking configurations considered, our calculations show that the most stable stacking for either polarization is identical, with the inner Te atom ( $\text{Te}_i$ ) sitting on the center of the top buckled hexagonal lattice of  $\text{In}_2\text{Se}_3$  [Figs. 1(a) and 1(c)] [34–36]. The interlayer distance increases from 2.54 to 2.67 Å when the polarization is switched from downward to upward, with other structural parameters staying intact, and the formation energies are 0.91 and 0.81 eV, respectively. The corresponding phonon spectra are further calculated [Figs. 1(b) and 1(d)], confirming their dynamical stability. The negligibly small imaginary frequencies near the  $\Gamma$  point for the upward case are an artifact of the simulations or lattice instabilities related to long wave undulations [37–39].

Before investigating the  $\text{IrTe}_2/\text{In}_2\text{Se}_3$  heterobilayers, we first calculate the EPC and  $T_c$  of  $\text{IrTe}_2$  nanoflakes to benchmark our methods. Since the  $\text{IrTe}_2$  nanoflakes are thick enough (e.g., 130–160 monolayers [15]), a bulk model is appropriate to mimic these nanoflakes. The total EPC strength ( $\lambda$ ) is calculated to be 0.76, with the three lowest-lying acoustic branches contributing 66% and the two lowest-lying optical branches also contributing substantially [40]. Using the McMillan-Allen-Dynes parametrized Eliashberg equation [30], we can estimate the  $T_c$  to be 2.99–4.48 K, with the Coulomb pseudopotential  $\mu^*$  taken as 0.15–0.10. These benchmark evaluations agree well with the experimentally observed  $T_c \sim 3.0$  K for  $\text{IrTe}_2$  nanoflakes [15,16], and

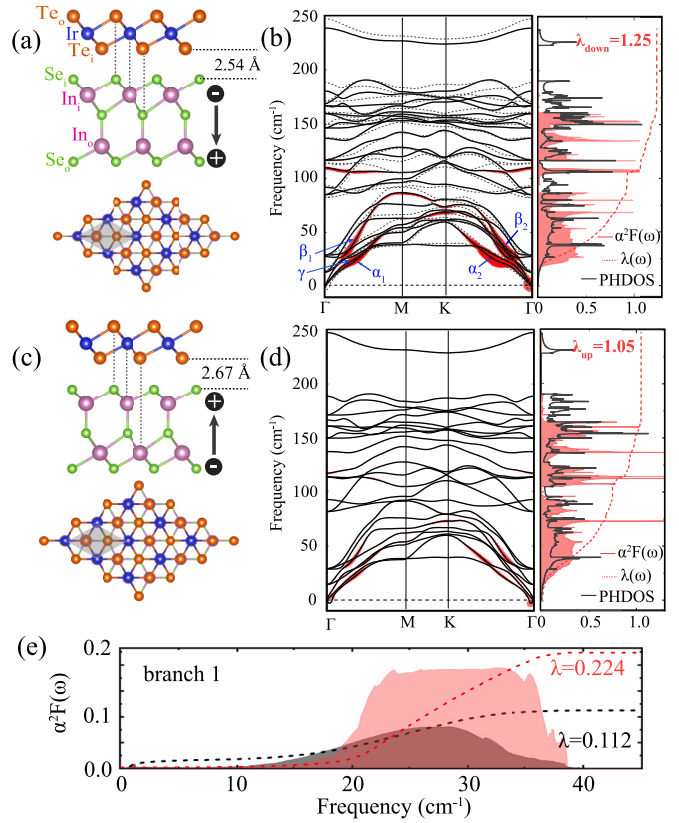


FIG. 1. Side and top views of an  $\text{IrTe}_2/\text{In}_2\text{Se}_3$  heterobilayer with (a) downward and (c) upward polarizations, with the unit cells highlighted. (b) Phonon spectra for the downward polarization, with the branch- and momentum-resolved EPC strengths indicated by the sizes of the red circles. The corresponding phonon density of states (PHDOS), Eliashberg function  $\alpha^2F(\omega)$ , and  $\lambda(\omega)$  are also shown. (d) Same as (b) but for the upward polarization, which is shown as the dashed lines in (b) as well. (e)  $\alpha^2F(\omega)$  and  $\lambda(\omega)$  for branch 1 for the downward (red) and upward (dark gray) polarizations.

the phonon spectra overall reproduce well the experimental Raman spectra [16,41,42]. Therefore, the adopted standard approaches within density functional theory (DFT) coupled with the isotropic superconducting picture are able to properly describe the  $\text{IrTe}_2$  systems. Furthermore, previous DFT plus dynamical mean field theory calculations have shown negligible electron correlation effects in bulk  $\text{IrTe}_2$  [43].

Next, we explore the ferroelectric field tuned EPC and  $T_c$  of the  $\text{IrTe}_2/\text{In}_2\text{Se}_3$  heterobilayers. The phonon spectra, Eliashberg function  $\alpha^2F(\omega)$ , and  $\lambda$  of the  $\text{IrTe}_2/\text{In}_2\text{Se}_3$  heterobilayers with opposite polarizations are given in Figs. 1(b) and 1(d). It is noted that the density of states at the Fermi level  $N(\varepsilon_F)$  of the heterobilayer with either polarization has been boosted by more than 60% from that of bulk  $\text{IrTe}_2$  (Table I), indicating significant charge repartitioning around the Fermi level. The enhanced  $N(\varepsilon_F)$  is also accompanied by the enhanced/emergent nesting. Such enhancements, in turn, play a vital role in enhancing the overall  $\lambda$ , where  $\lambda$  is proportional to  $N(\varepsilon_F)$  [44], provided that other parameters are kept unchanged. More intriguingly, the  $T_c$  of the heterobilayer for the downward polarization is higher than that for the upward case. The calculated partial charges for both

TABLE I. Density of states at the Fermi level  $N(\varepsilon_F)$ , logarithmic average of the phonon frequencies  $\omega_{\log}$ , total EPC strength  $\lambda$ , and superconducting transition temperature  $T_c$  of bulk IrTe<sub>2</sub> and IrTe<sub>2</sub>/In<sub>2</sub>Se<sub>3</sub> heterobilayers.

System	$N(\varepsilon_F)$ (Ry <sup>-1</sup> )	$\omega_{\log}$ (K)	$\lambda$	$T_c$ (K) $\mu^* = 0.15\text{--}0.10$
Bulk IrTe <sub>2</sub>	12.27	105.43	0.76	2.99–4.48 ( $\sim 3.0^a$ )
IrTe <sub>2</sub> /In <sub>2</sub> Se <sub>3</sub> ↓	20.88	92.33	1.25	7.70–9.58
IrTe <sub>2</sub> /In <sub>2</sub> Se <sub>3</sub> ↑	19.68	88.53	1.05	5.48–7.14

<sup>a</sup>Experimental values [15,16].

polarizations around the Fermi level show that the charge more noticeably pervades in the interlayer space for the downward case [Fig. 2(a)]; accordingly, the interlayer vibrational modes are more likely to influence these states, contribute to the  $\lambda$ , and enhance  $T_c$ . At a branch-specific level, the eight low-frequency phonon branches have been softened for the downward polarization as compared with the upward case [Fig. 1(b)]. Their corresponding contributions to the EPC strengths are 0.93 and 0.74, while the remaining 16 branches collectively contribute an equal EPC strength of 0.30 for both cases [40].

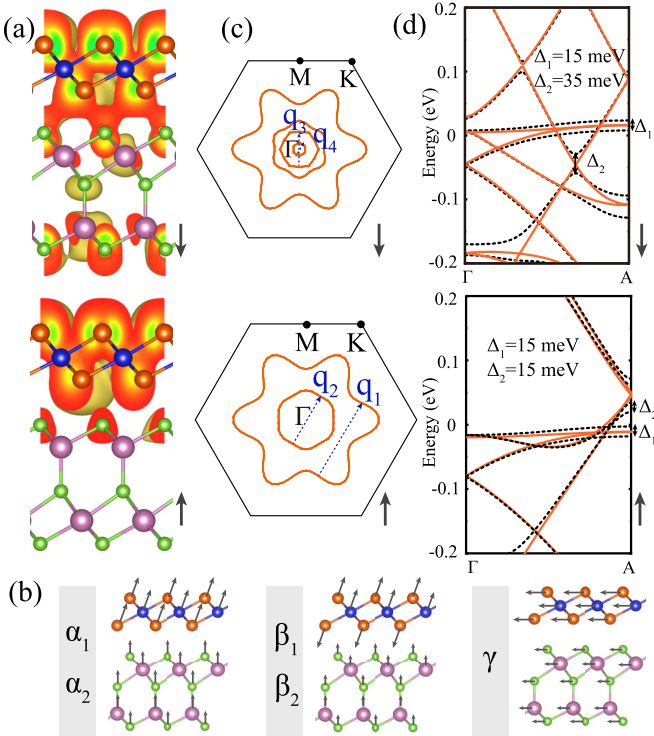


FIG. 2. (a) Partial charge distributions within  $(-0.05, 0.05)$  eV for the downward ( $\downarrow$ ) and upward ( $\uparrow$ ) polarizations, adopting the same isosurface values. (b) Illustrations of the atomic displacements for phonon modes  $\alpha_1$ ,  $\alpha_2$ ,  $\beta_1$ ,  $\beta_2$ , and  $\gamma$ . (c) Fermi surfaces without the SOC, with nesting vectors  $\mathbf{q}_1$ ,  $\mathbf{q}_2$ ,  $\mathbf{q}_3$ , and  $\mathbf{q}_4$  indicated. (d) Band structures of a  $6 \times 1 \times 1$  supercell before (solid lines) and after (dashed lines) the lattice distortion caused by mode  $\alpha_1$ , with  $\Gamma$  and A denoting the center and midpoint of the longer margin of the Brillouin zone and  $\Delta$  denoting the band splittings.

Given the above analyses, we focus on the eight low-frequency branches to explore the physical origins of the different  $\lambda$ 's in the two polarizations. The Fermi surface of the upward-polarized structure is composed of a large flowerlike hole pocket and a smaller hexagonal hole pocket, providing strong Fermi nesting of the electrons [ $\mathbf{q}_1$ ,  $\mathbf{q}_2$ , and their  $60^\circ$  and  $120^\circ$  rotations in Fig. 2(c)]. For the downward case, additional hexagonal hole pockets centered at the  $\Gamma$  point are introduced with nesting vectors being  $\mathbf{q}_3$ ,  $\mathbf{q}_4$ , and their counterparts. Furthermore, the branch ( $\nu$ )- and momentum ( $\mathbf{q}$ )-resolved  $\lambda_{\mathbf{q}\nu}$ 's are indicated by the sizes of the red circles in Figs. 1(b) and 1(d). The most prominent  $\lambda_{\mathbf{q}\nu}$ 's lie between  $(1/4\text{--}3/4)$  regions along the  $\Gamma K$  and  $\Gamma M$  directions, corresponding to the well-defined nesting vectors  $\mathbf{q}_1$  and  $\mathbf{q}_2$  along  $\Gamma K$  and EPC-involved phonon momenta along  $\Gamma M$ . In particular, the five phonon modes ( $\alpha_1$ ,  $\alpha_2$ ,  $\beta_1$ ,  $\beta_2$ , and  $\gamma$ ) depicted in Fig. 2(b) significantly enhance the EPC when the polarization direction changes. Here,  $\alpha_1$ ,  $\alpha_2$ ,  $\beta_1$ , and  $\beta_2$  are mainly associated with the interlayer out of plane vibrations (mixed with the IrTe<sub>2</sub> intralayer vibrations in  $\beta_1$  and  $\beta_2$ ), while  $\gamma$  is dominated by the interlayer in-plane vibrations. In addition, our branch-resolved  $\lambda$  calculations show that the most striking enhancement in  $\lambda$  originates from branch 1, from 0.112 (upward) to 0.224 (downward), accounting for 50% of the total EPC increase [Fig. 1(e)]. Besides, the total contribution from branches 2–8 is also enhanced [40], collectively resulting in a moderate increase in  $\lambda$ . Among the eight phonon branches, 2–8 are insensitive to the interlayer coupling; assuming a common EPC matrix, the enhanced EPC of these branches can be mainly attributed to the slight increases in  $N(\varepsilon_F)$  and the phonon softening [40].

To decipher the underlying mechanism of the branch-1 enhanced  $\lambda$ , we analyze the  $\lambda_{\mathbf{q}\nu}$  by investigating the EPC matrix whose elements can be inferred from the shifts of energy bands in a frozen phonon calculation [45]. The band structures before and after the distortion by the selective interlayer vibration  $\alpha_1$  of branch 1 at  $\frac{1}{3}\Gamma M$  are calculated using a commensurate  $6 \times 1 \times 1$  supercell [Fig. 2(d)]. With the atom displacement of  $0.05 \text{ \AA}$ , the band degeneracies at the A point are lifted. Since the  $\lambda_{\mathbf{q}\nu}$  is approximately proportional to the square of the band splittings in the frozen phonon calculation [45], we obtain that the ratio of the average splitting energies between the downward and upward polarizations is 1.5, leading to a  $\lambda_{\mathbf{q}\nu}$  enhancement by a factor of  $\sim 2.3$ , consistent with our density functional perturbation theory calculations. Therefore, when the polarization is switched from upward to downward, the pronounced enhancement of the  $\lambda$  from branch 1 originates from the enhanced interlayer electron-phonon coupling.

At this point, it is worthwhile to emphasize four aspects related to the superconducting results. First, given the concentric-circle-like electronic Fermi surfaces and nearly isotropic phonon dispersions along the  $\Gamma M$  and  $\Gamma K$  directions, the adoption of the isotropic Eliashberg equation can be well justified. Secondly, to justify the non-SOC calculations, we have compared the EPC strengths of bulk IrTe<sub>2</sub> at the  $\Gamma$  point with and without the SOC, showing a negligible difference of less than 1%. In any case, the central physical aspect that the polarity can tune the  $T_c$  is expected to stay intact whether the SOC effect is fully accounted for or not. Thirdly,

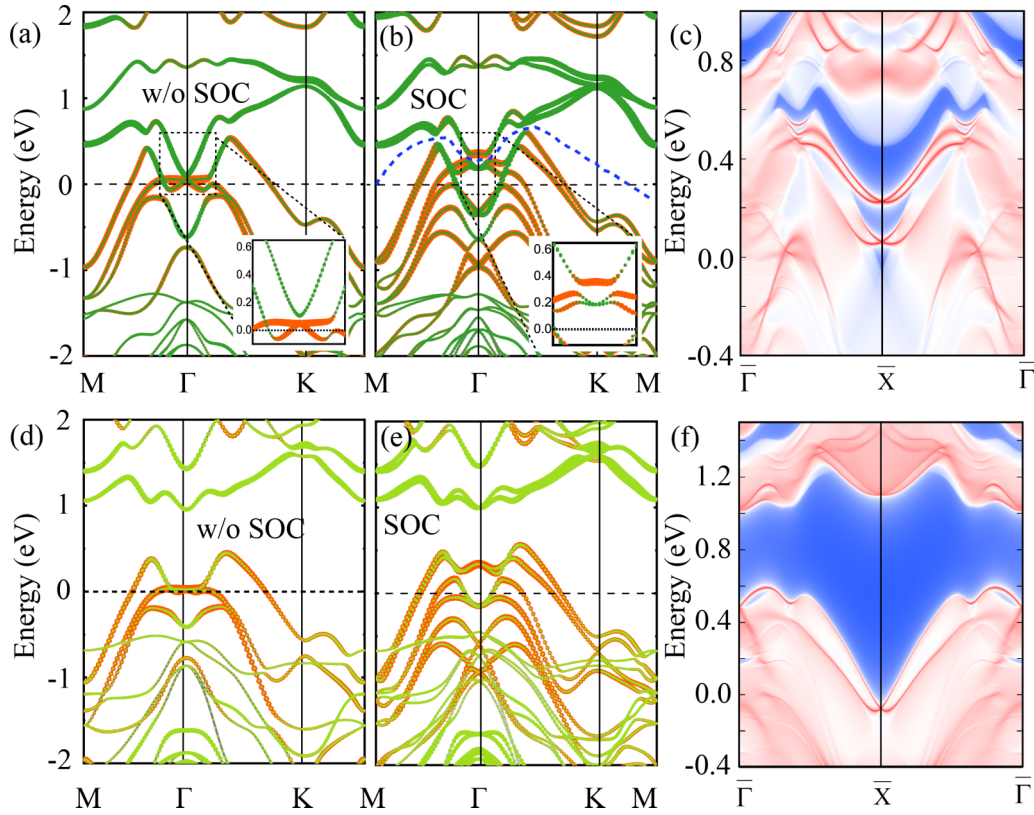


FIG. 3. Band structures for the downward polarization calculated (a) without and (b) with the SOC. The insets are the zoomed-in views. (c) Edge states of the corresponding semi-infinite slab with Te and Se terminations along the zigzag direction, with  $\bar{\Gamma}$  and  $\bar{X}$  in the 1D Brillouin zone of the slab. The warmer colors denote higher density of states, and the blue regions denote the bulk band gaps. (d)–(f) Same as (a)–(c) but for the upward polarization. In (a), (b), (d), (e), the sizes of the dark green, light green, and orange circles indicate the contributions from the  $\text{In}_o + \text{Se}_o$ ,  $\text{In}_i + \text{Se}_i$ , and  $\text{Te}-p$  orbitals, respectively.

unlike the carrier doping mechanism in traditional superconductor/ferroelectric heterostructures [3–5] or ferroelectrics [46], the present mechanism of ferroelectric-enhanced  $T_c$  is mainly attributed to enhanced interfacial electron-phonon coupling. Here the switching of polarization determines whether the interlayer electrons and interlayer phonons (more specifically, the  $\alpha_1$ ,  $\alpha_2$ ,  $\beta_1$ ,  $\beta_2$ , and  $\gamma$  modes) are actively invoked in the EPC process. Such a mechanism bears a resemblance to the basic physics of twisted bilayer graphene, where superconductivity emerges due to interlayer states [47]. Fourthly and most importantly, the multiply nested Fermi surface may lead to various types of superconducting orders and particle-hole instabilities. Yet for the  $\text{IrTe}_2/\text{In}_2\text{Se}_3$  heterobilayer, since the phonon-mediated attraction overwhelms Coulomb repulsion in the  $s$ -wave channel due to strong EPC strengths, a superconducting order with zero  $\mathbf{q}$  and opposite spin pairings is therefore more likely to be selected. Even though extensive studies have revealed the interplay between different charge orderings and superconductivity in bulk and thin-flake  $\text{IrTe}_2$  [15,42,43,48–50], here we emphasize that no imaginary phonon is present with either polarization, indicating the absence of charge density wave in the heterobilayer. Moreover, several pure electronic instabilities have been analyzed in detail for these heterobilayers [40], which can be ruled out as well.

Finally, we investigate the ferroelectric switching of band topology in the  $\text{IrTe}_2/\text{In}_2\text{Se}_3$  heterobilayers. The different fer-

roelectric polarizations can induce different band alignments and charge transfer between the  $\text{IrTe}_2$  and  $\text{In}_2\text{Se}_3$  monolayers, which may play a role in controlling the topological band character of the heterobilayers. Figures 3(a), 3(b), 3(d), and 3(e) show the projected band structures of the  $\text{IrTe}_2/\text{In}_2\text{Se}_3$  heterobilayers for both polarizations without and with the SOC. For the downward polarization, although there is no global gap, a local gap exists at every point in the whole Brillouin zone. By introducing a “curved chemical potential” [the blue dashed line in Fig. 3(b)] through the local gap [51], the topological invariant  $Z_2$  for time-reversal invariant systems can be well defined [52], and the band inversions can also be analyzed. Specifically, without the SOC, there exists a small gap of  $\sim 55$  meV between the  $\text{In}_o + \text{Se}_o$  and  $\text{Te}-p$  bands around the  $\Gamma$  point [Fig. 3(a)]. When the SOC is included, the  $\text{In}_o + \text{Se}_o$  and  $\text{Te}-p$  bands are inverted by crossing the curved chemical potential [Fig. 3(b)], which may be accompanied by a topological phase transition. In contrast, for the upward polarization, there is a global gap above the Fermi level, with 0.93 eV around the  $\Gamma$  point. The SOC can reduce the gap, but cannot close it to induce a band inversion [Fig. 3(e)], resulting in a trivial state.

We then calculate the topological invariant  $Z_2$  using the Wannier charge center (WCC) method [52]. For the downward polarization, an odd number of times of WCC crossing with any arbitrary horizontal reference line is observed, revealing a topologically nontrivial state ( $Z_2 = 1$ ). The non-

trivial topology is further shown to be rather robust, persisting when subjecting the system to a compressive biaxial strain of 5% or in a metastable configuration [40]. In contrast, an even number of times of WCC crossing is observed in the upward-polarization case, leading to its trivial character ( $Z_2 = 0$ ). Note that, depending on the specific materials combinations of the ferroelectric/superconductor heterostructures, it is expected that different band topologies will be realized for different functionalities. As another manifestation of the nontrivial band topology, the edge states of a semi-infinite slab with Te and Se terminations along the zigzag direction are calculated for both polarizations [Figs. 3(c) and 3(f)]. A pair of topological edge states with Dirac nature at the  $\bar{X}$  point is observed within the bulk gap for the downward case, while it is absent for the upward case. These topological edge states are located in the energy window where there also exist multiple bulk bands, and the two can be differentiated by their different responses to chemical passivation [53].

Given that different choices of the vdW corrections for the interlayer coupling, the robustness of the main findings using the PBE-D2 scheme in this study should be checked. Indeed, essentially all the calculations using the vdW-optB86b functional [54] have been repeated in Ref. [40], showing that the main results, namely, the ferroelectric nature of  $\text{In}_2\text{Se}_3$  and the dual tunabilities in the band topology and  $T_c$ , stay intact.

Before closing, we briefly discuss several aspects related to realizations and potential applications of the strong and intriguing predictions made here. First, on the sample preparation, since  $\text{In}_2\text{Se}_3$  monolayers have been widely fabricated [11,55], we suggest to use  $\text{In}_2\text{Se}_3$  as the substrate and transfer or epitaxially grow  $\text{IrTe}_2$  monolayers. Our calculations have shown that  $\text{In}_2\text{Se}_3$  can help to stabilize the  $\text{IrTe}_2$  monolayer (in contrast, the phonon spectra of an  $\text{IrTe}_2$  monolayer show significant imaginary frequencies [56]). Secondly, on the aspect of polarization reversal, our calculated energy barrier of an  $\text{IrTe}_2/\text{In}_2\text{Se}_3$  heterobilayer against polarization flipping from upward to downward is 0.11 eV, slightly higher than that of a freestanding  $\text{In}_2\text{Se}_3$  monolayer (0.08 eV). In addition, domain wall motion barriers in the heterobilayer are lower than that in pristine  $\text{In}_2\text{Se}_3$  [40], indicating easier polarization reversibility in the former. Thirdly, materials possessing dual tunabilities in band topology and superconductivity are very rare. Even though the 2D bulk superconducting state is not topological for downward polarization, given the co-existence of *s*-wave superconductivity and nontrivial band topology, one-dimensional (1D) topological superconductivity or Majorana zero modes (MZMs) can be observed via the self-proximity effect [57–59]. As the MZMs are confined at

the boundaries of topologically nontrivial and trivial domains in the  $\text{IrTe}_2/\text{In}_2\text{Se}_3$  heterobilayer, the spatial locations of such MZMs can be readily manipulated via the intrinsic ferroelectric polarization, a crucial step, if achieved, in gaining the controlled interaction of multiple MZMs and ultimately their braiding. Finally, the concept of a 2D heterobilayer with tunable/switchable  $T_c$  should also provide appealing building blocks for developing next-generation nanoscale superconducting devices such as superconducting diodes [60].

In conclusion, we have demonstrated a simultaneous tuning of  $T_c$  and band topology by ferroelectric polarization in the  $\text{IrTe}_2/\text{In}_2\text{Se}_3$  heterobilayers. The opposite polarizations cause different band alignments and charge transfer between the  $\text{In}_2\text{Se}_3$  and  $\text{IrTe}_2$  monolayers when forming the heterobilayers, which play a vital role in enhancing the  $T_c$  and inverting the electronic bands. In particular, when the polarization is downward, the charge transfers significantly from the  $\text{IrTe}_2$  and accumulates at the interface, resulting in stronger electron-phonon coupling that accounts for the higher  $T_c$ . This downward configuration is also accompanied by the emergence of nontrivial band topology. This study not only showcases a distinct and unprecedented approach to simultaneously tune superconductivity and band topology, but also sheds light on the underlying mechanisms of ferroelectric field induced superconductivity in 2D heterostructures.

*Note added.* After the submission of this paper, two groups have reported experimental demonstrations of the bistable switching of superconducting states in properly fabricated 2D heterostructures invoking bilayer  $\text{MoTe}_2$  [61] or bilayer graphene [62] via 2D ferroelectric control. Given the property versatilities of these systems, we expect that the tunability of the topological properties of such 2D superconductors by 2D ferroelectricity as predicted here will soon be demonstrated as well.

We thank Prof. Fuchun Zhang, Dr. Lei qiang Li, and Dr. Wenjun Ding for helpful discussions. This work was supported by the Innovation Program for Quantum Science and Technology (Grant No. 2021ZD0302800), the National Natural Science Foundation of China (Grants No. 11974323 and No. 12204121), the National Key R&D Program of China (Grant No. 2017YFA0303500), the Anhui Initiative in Quantum Information Technologies (Grant No. AHY170000), and the Strategic Priority Research Program of Chinese Academy of Sciences (Grant No. XDB30000000). J.C. also acknowledges the support from the Guangxi Natural Science Foundation (Grants No. 2019GXNSFBA245077 and No. 2021GXNSFAA220129).

[1] J. E. Villegas, S. Savel'ev, F. Nori, E. M. Gonzalez, J. V. Anguita, R. García, and J. L. Vicent, *Science* **302**, 1188 (2003).  
 [2] S. Ooi, S. Savel'ev, M. B. Gaifullin, T. Mochiku, K. Hirata, and F. Nori, *Phys. Rev. Lett.* **99**, 207003 (2007).  
 [3] C. H. Ahn, S. Gariglio, P. Paruch, T. Tybell, L. Antognazza, and J. M. Triscone, *Science* **284**, 1152 (1999).  
 [4] A. Crassous, R. Bernard, S. Fusil, K. Bouzehouane, D. Le Bourdais, S. Enouz-Vedrenne, J. Briatico, M. Bibes, A.

Barthélémy, and J. E. Villegas, *Phys. Rev. Lett.* **107**, 247002 (2011).

[5] K. S. Takahashi, M. Gabay, D. Jaccard, K. Shibuya, T. Ohnishi, M. Lippmaa, and J. M. Triscone, *Nature (London)* **441**, 195 (2006).  
 [6] N. Reyren, S. Thiel, A. D. Caviglia, L. F. Kourkoutis, G. Hammerl, C. Richter, C. W. Schneider, T. Kopp, A. S. Rüetschi, and D. Jaccard, *Science* **317**, 1196 (2007).

- [7] Z. Chen, Z. Liu, Y. Sun, X. Chen, Y. Liu, H. Zhang, H. Li, M. Zhang, S. Hong, and T. Ren, *Phys. Rev. Lett.* **126**, 026802 (2021).
- [8] C. A. F. Vaz, Y. J. Shin, M. Bibes, K. M. Rabe, F. J. Walker, and C. H. Ahn, *Appl. Phys. Rev.* **8**, 041308 (2021).
- [9] F. Liu, L. You, K. L. Seyler, X. Li, P. Yu, J. Lin, X. Wang, J. Zhou, H. Wang, H. He *et al.*, *Nat. Commun.* **7**, 12357 (2016).
- [10] K. Chang, J. Liu, H. Lin, N. Wang, K. Zhao, A. Zhang, F. Jin, Y. Zhong, X. Hu, and W. Duan, *Science* **353**, 274 (2016).
- [11] F. Xue, W. Hu, K. C. Lee, L. S. Lu, J. Zhang, H. L. Tang, A. Han, W. T. Hsu, S. Tu, and W. H. Chang, *Adv. Func. Mater.* **28**, 1803738 (2018).
- [12] S. Yuan, X. Luo, H. L. Chan, C. Xiao, Y. Dai, M. Xie, and J. Hao, *Nat. Commun.* **10**, 1775 (2019).
- [13] W. Ding, J. Zhu, Z. Wang, Y. Gao, D. Xiao, Y. Gu, Z. Zhang, and W. Zhu, *Nat. Commun.* **8**, 14956 (2017).
- [14] J. Xiao, H. Zhu, Y. Wang, W. Feng, Y. Hu, A. Dasgupta, Y. Han, Y. Wang, D. A. Muller, L. W. Martin *et al.*, *Phys. Rev. Lett.* **120**, 227601 (2018).
- [15] M. Yoshida, K. Kudo, M. Nohara, and Y. Iwasa, *Nano Lett.* **18**, 3113 (2018).
- [16] Y. Song, F. Meng, T. Ying, J. Deng, J. Wang, X. Han, Q. Zhang, Y. Huang, J.-g. Guo, and X. Chen, *J. Phys. Chem. Lett.* **12**, 12180 (2021).
- [17] X. Xi, Z. Wang, W. Zhao, J.-H. Park, K. T. Law, H. Berger, L. Forró, J. Shan, and K. F. Mak, *Nat. Phys.* **12**, 139 (2016).
- [18] C. Xu, L. Wang, Z. Liu, L. Chen, J. Guo, N. Kang, X.-L. Ma, H.-M. Cheng, and W. Ren, *Nat. Mater.* **14**, 1135 (2015).
- [19] J. Li, X. Yang, Y. Liu, B. Huang, R. Wu, Z. Zhang, B. Zhao, H. Ma, W. Dang, and Z. Wei, *Nature (London)* **579**, 368 (2020).
- [20] X. Zhou and G. Yu, *ACS Nano* **15**, 11040 (2021).
- [21] P. Giannozzi, S. Baroni, N. Bonini, M. Calandra, R. Car, C. Cavazzoni, D. Ceresoli, G. L. Chiarotti, M. Cococcioni, I. Dabo *et al.*, *J. Phys.: Condens. Matter* **21**, 395502 (2009).
- [22] J. P. Perdew, K. Burke, and M. Ernzerhof, *Phys. Rev. Lett.* **77**, 3865 (1996).
- [23] S. Grimme, J. Antony, S. Ehrlich, and H. Krieg, *J. Chem. Phys.* **132**, 154104 (2010).
- [24] S. Grimme, *J. Comput. Chem* **27**, 1787 (2006).
- [25] V. Barone, M. Casarin, D. Forrer, M. Pavone, M. Sambri, and A. Vittadini, *J. Comput. Chem* **30**, 934 (2009).
- [26] S. Baroni, S. de Gironcoli, A. Dal Corso, and P. Giannozzi, *Rev. Mod. Phys.* **73**, 515 (2001).
- [27] M. Methfessel and A. T. Paxton, *Phys. Rev. B* **40**, 3616 (1989).
- [28] N. Marzari, D. Vanderbilt, A. De Vita, and M. C. Payne, *Phys. Rev. Lett.* **82**, 3296 (1999).
- [29] P. B. Allen, *Phys. Rev. B* **6**, 2577 (1972).
- [30] P. B. Allen and R. C. Dynes, *Phys. Rev. B* **12**, 905 (1975).
- [31] M. P. Lopez Sancho, J. M. Lopez Sancho, J. M. L. Sancho, and J. Rubio, *J. Phys. F: Met. Phys.* **15**, 851 (1985).
- [32] A. A. Mostofi, J. R. Yates, Y.-S. Lee, I. Souza, D. Vanderbilt, and N. Marzari, *Comput. Phys. Commun.* **178**, 685 (2008).
- [33] Q. Wu, S. Zhang, H.-F. Song, M. Troyer, and A. A. Soluyanov, *Comput. Phys. Commun.* **224**, 405 (2018).
- [34] J.-J. Zhang, D. Zhu, and B. I. Yakobson, *Nano Lett.* **21**, 785 (2021).
- [35] H. Bai, X. Wang, W. Wu, P. He, Z. Xu, S. A. Yang, and Y. Lu, *Phys. Rev. B* **102**, 235403 (2020).
- [36] M. Wu and J. Li, *Proc. Natl. Acad. Sci. USA* **118**, e2115703118 (2021).
- [37] A. H. Castro Neto, F. Guinea, N. M. R. Peres, K. S. Novoselov, and A. K. Geim, *Rev. Mod. Phys.* **81**, 109 (2009).
- [38] S. Cahangirov, M. Topsakal, E. Aktürk, H. Şahin, and S. Ciraci, *Phys. Rev. Lett.* **102**, 236804 (2009).
- [39] E. S. Penev, A. Kutana, and B. I. Yakobson, *Nano Lett.* **16**, 2522 (2016).
- [40] J. Chen, W. Qin, P. Cui, and Z. Zhang, companion paper, *Phys. Rev. B* **108**, 085408 (2023).
- [41] H. Oike, K. Takeda, M. Kamitani, Y. Tokura, and F. Kagawa, *Phys. Rev. Lett.* **127**, 145701 (2021).
- [42] S. Park, S. Y. Kim, H. K. Kim, M. J. Kim, T. Kim, H. Kim, G. S. Choi, C. J. Won, S. Kim, K. Kim *et al.*, *Nat. Commun.* **12**, 3157 (2021).
- [43] G.-L. Pascut, K. Haule, M. J. Gutmann, S. A. Barnett, A. Bombardi, S. Artyukhin, T. Birol, D. Vanderbilt, J. J. Yang, S. W. Cheong *et al.*, *Phys. Rev. Lett.* **112**, 086402 (2014).
- [44] G. Profeta, M. Calandra, and F. Mauri, *Nat. Phys.* **8**, 131 (2012).
- [45] Z. P. Yin, A. Kutepov, and G. Kotliar, *Phys. Rev. X* **3**, 021011 (2013).
- [46] J. Ma, R. Yang, and H. Chen, *Nat. Commun.* **12**, 2314 (2021).
- [47] Y. Cao, V. Fatemi, S. Fang, K. Watanabe, T. Taniguchi, E. Kaxiras, and P. Jarillo-Herrero, *Nature (London)* **556**, 43 (2018).
- [48] H. S. Kim, S. Kim, K. Kim, B. I. Min, Y.-H. Cho, L. Wang, S.-W. Cheong, and H. W. Yeom, *Nano Lett.* **16**, 4260 (2016).
- [49] J. J. Yang, Y. J. Choi, Y. S. Oh, A. Hogan, Y. Horibe, K. Kim, B. I. Min, and S.-W. Cheong, *Phys. Rev. Lett.* **108**, 116402 (2012).
- [50] G. Saleh and S. Artyukhin, *J. Phys. Chem. Lett.* **11**, 2127 (2020).
- [51] Z. Wang, P. Zhang, G. Xu, L. K. Zeng, H. Miao, X. Xu, T. Qian, H. Weng, P. Richard, A. V. Fedorov *et al.*, *Phys. Rev. B* **92**, 115119 (2015).
- [52] A. A. Soluyanov and D. Vanderbilt, *Phys. Rev. B* **83**, 235401 (2011).
- [53] C. Zhao, L. Li, L. Zhang, J. Qin, H. Chen, B. Xia, B. Yang, H. Zheng, S. Wang, C. Liu *et al.*, *Phys. Rev. Lett.* **128**, 206802 (2022).
- [54] J. Klimeš, D. R. Bowler, and A. Michaelides, *Phys. Rev. B* **83**, 195131 (2011).
- [55] F. Zhang, Z. Wang, L. Liu, A. Nie, Y. Gong, W. Zhu, and C. Tao, *J. Phys. Chem. Lett.* **12**, 11902 (2021).
- [56] X. Li, F. Liu, and Q. Wang, *Phys. Rev. B* **102**, 195420 (2020).
- [57] L. Fu and C. L. Kane, *Phys. Rev. Lett.* **100**, 096407 (2008).
- [58] J. Alicea, *Rep. Prog. Phys.* **75**, 076501 (2012).
- [59] P. Zhang, K. Yaji, T. Hashimoto, Y. Ota, T. Kondo, K. Okazaki, Z. Wang, J. Wen, G. D. Gu, H. Ding *et al.*, *Science* **360**, 182 (2018).
- [60] H. Wu, Y. Wang, Y. Xu, P. K. Sivakumar, C. Pasco, U. Filippozzi, S. S. P. Parkin, Y.-J. Zeng, T. McQueen, and M. N. Ali, *Nature (London)* **604**, 653 (2022).
- [61] A. Jindal, A. Saha, Z. Li, T. Taniguchi, K. Watanabe, J. C. Hone, T. Birol, R. M. Fernandes, C. R. Dean, A. N. Pasupathy *et al.*, *Nature (London)* **613**, 48 (2023).
- [62] D. R. Klein, L.-Q. Xia, D. MacNeill, K. Watanabe, T. Taniguchi, and P. Jarillo-Herrero, *Nat. Nanotechnol.* **18**, 331 (2023).